PNAS RESEARCH ARTICLE | NEUROSCIENCE

The neural bases of the reach–grasp movement in humans: Quantitative evidence from brain lesions

Valeria Di Caro[a], Paola Cesari[b], Francesco Sala[a,1], and Luigi Cattaneo[c,d,1,2]

Edited by Peter Strick, University of Pittsburgh Brain Institute, Pittsburgh, PA; received September 26, 2024; accepted January 27, 2025

Visually guided grasping is a fundamental building block of animal behavior, the specific neural mechanisms of which remain poorly documented in the human brain. We have mapped the causal contribution of different brain parts to grasping behavior by studying the kinematic parameters of 33 patients with brain tumors, engaged in actions directed toward objects of different sizes. Using motion capture techniques, we analyzed the dynamics of grip aperture and wrist transport. Voxel-based lesion-symptom mapping analysis was applied to correlate lesion volumes with specific behavioral deficits. Results showed that lesions in the anterior and lateral bank of the intraparietal sulcus produced impaired finger scaling related to object size. Conversely, impaired velocity of finger aperture was associated with lesions in the dorsal premotor cortex (PMd). Grip aperture deficits following dominant hemisphere lesions were bilateral and were unilateral when following nondominant hemisphere lesions. Impaired wrist transport during reaching was associated with lesions in the first segment of the superior longitudinal fasciculus. Our work highlights an architecture of the grasping network in humans, with unique species-specific features. We hypothesize a model of human neural architecture in which object geometry for hand preshaping is first coded in the left anterior intraparietal cortex and then shared with the right hemisphere. Execution of the motor program of hand preshaping is then performed by the PMd on the corresponding side.

grasping | reaching | premotor | parietal | visuomotor

Significance

Visually guided grasping is a fundamental building block of animal behavior, the specific neural mechanisms of which remain poorly documented in the human brain. We have mapped the causal contribution of different brain parts to grasping behavior in patients with brain tumors. We found evidence for a human-specific neural architecture of the reach–grasp network, in which object geometry for hand preshaping is first coded in the left anterior intraparietal cortex and then shared with the right hemisphere. Execution of the motor program of hand preshaping is then performed by the dorsal premotor cortex on the corresponding side.

Reaching and grasping a visible target is a basic building block of animal behavior. The nervous systems and bodies of different invertebrates and vertebrates developed reach–grasp behavior with different mechanisms (1). In primates, according to a widely agreed-upon model, the reach–grasp movement is mainly represented at the cortical level (2). Visual and multisensory information on action targets is mapped in specific and largely segregated parieto-frontal circuits that perform sensorimotor transformations (3). In nonhuman primates, visually guided grasping is supported by a specific ventral circuit, known as the "grasping circuit" (4), comprising the anterior intraparietal area (AIP), which is connected to different portions of the premotor cortex and more specifically to a section of the ventral premotor cortex (PMv) referred to as areas F5a and F5p, which occupy the caudal bank of the arcuate sulcus (5) but also, although to a lesser extent, to the dorsal and medial premotor cortices (6). The grasping circuit is thought to use visual information about target objects to configure the shape of the hand and fingers appropriately during the reaching phase (7) and is therefore mainly active before actually touching the object. Conversely, once contact has been made and actual holding/manipulation occurs, the motor system tunes instead to somatosensory/haptic information (8–10). The functional properties of neurons in the grasping circuit have been extensively studied in monkeys: both the parietal and the premotor nodes of the circuit contain neurons that respond to visual stimuli and that are selective for the objects' shapes and affordances and that also fire during the movement directed toward the corresponding object (10–12). Though sensorimotor neurons are found in both AIP and F5, the population of neurons in the parietal cortex is more tuned to the visual modality (13–16) and the premotor population is more tuned to motor representation (10, 12). The existence of object-specific visuomotor neurons in monkeys has led to the concept of "vocabulary of motor acts" (17) stored in the PMv of primates, meaning that the PMv contains a limited series of object-dependent motor synergies, that account for most of the motor repertoire, though more recent multiunit analyses have shown that the PMv does not represent only invariant object geometry, but also shows activity dependent on object position, orientation, used body part, and lower-level kinematic parameters as grasp force (10, 18, 19). Finally, there is anatomical (20) and physiological (21, 22) evidence in the macaque, that the access to motor output of the circuit is mainly mediated by premotor-motor corticocortical connections, though the existence of direct parietal-motor connections of uncertain significance is admitted in both monkeys and humans (23–25).

Author affiliations: [a]Section of Neurosurgery, Department of Neurosciences, Biomedicine and Movement Sciences, University of Verona, Verona 37134, Italy; [b]Section of Movement Sciences, Department of Neurosciences, Biomedicine and Movement Sciences, University of Verona, Verona 37134, Italy; [c]Center for Mind/Brain Sciences, University of Trento, Trento 38123, Italy; and [d]Center for Medical Sciences, University of Trento, Trento 38122, Italy

Author contributions: V.D.C., P.C., F.S., and L.C. designed research; V.D.C., F.S., and L.C. performed research; V.D.C., P.C., F.S., and L.C. analyzed data; and V.D.C., P.C., F.S., and L.C. wrote the paper.

The authors declare no competing interest.

This article is a PNAS Direct Submission.

[1]F.S. and L.C. contributed equally to this work.

[2]To whom correspondence may be addressed. Email: luigi.cattaneo@unitn.it.

This article contains supporting information online at https://www.pnas.org/lookup/suppl/doi:10.1073/pnas.2419801122/-/DCSupplemental.

Published March 5, 2025.

In humans, neuroimaging studies indicate that the geometric properties of objects to be grasped are strongly represented in the anterior intraparietal region, which will be referred to as the putative human AIP (phAIP) (26–28). Unlike the robust activity observed in phAIP, imaging studies have generally failed to show strong consistent object-related activity in the human ventral premotor region. However, noninvasive brain stimulation findings show that the ventral premotor region is indeed functionally connected to M1 during visually guided grasping (9, 29–31). Robust causal information on the anatomy of the human grasping circuit coming from lesional studies in humans is very limited. Human premotor lesions do not seem to cause overt visuomotor deficits according to one case series (32), while phAIP lesions have been shown to cause specific visuomotor impairments in a series of 4 patients (33). Summing up, the functional anatomy of the grasping circuit in humans is still far from being clarified and further studies coupling anatomical information and causal functional information are required.

Though some previous work has documented that hand preshaping during hand transport is sensitive to brain lesions in monkeys (11, 34) and in humans (33, 35), no work has, to date, assessed the relation between specific lesion localizations in the human brain and specific deficits in the reach–grasp behavior in a significantly large population of patients with controlled statistical methods. In the present work, we aim to fill this gap in neuroscientific knowledge. To do so, we recruited patients with single supratentorial brain tumoral lesions, undergoing elective surgery for tumor removal. Prior to surgery, we recorded upper limb kinematics during a reach–grasp–lift behavior directed at two real objects (a 5 cm and a 8 cm diameter spheres) in a behavioral task that has been previously validated to be sensitive to transient alterations in brain functions (36). A schematic of the movement is represented in Fig. 1*A*. To measure motor performance, we used motion capture procedures (37), which represent the gold-standard procedure to measure movement. These consist of placing markers on different body parts, the position of which is continuously sensed by optical or ultrasound-based systems, by which we can reconstruct the reciprocal position of body parts, joint angles, and kinematic parameters such as velocity or acceleration. We extracted several features of movement

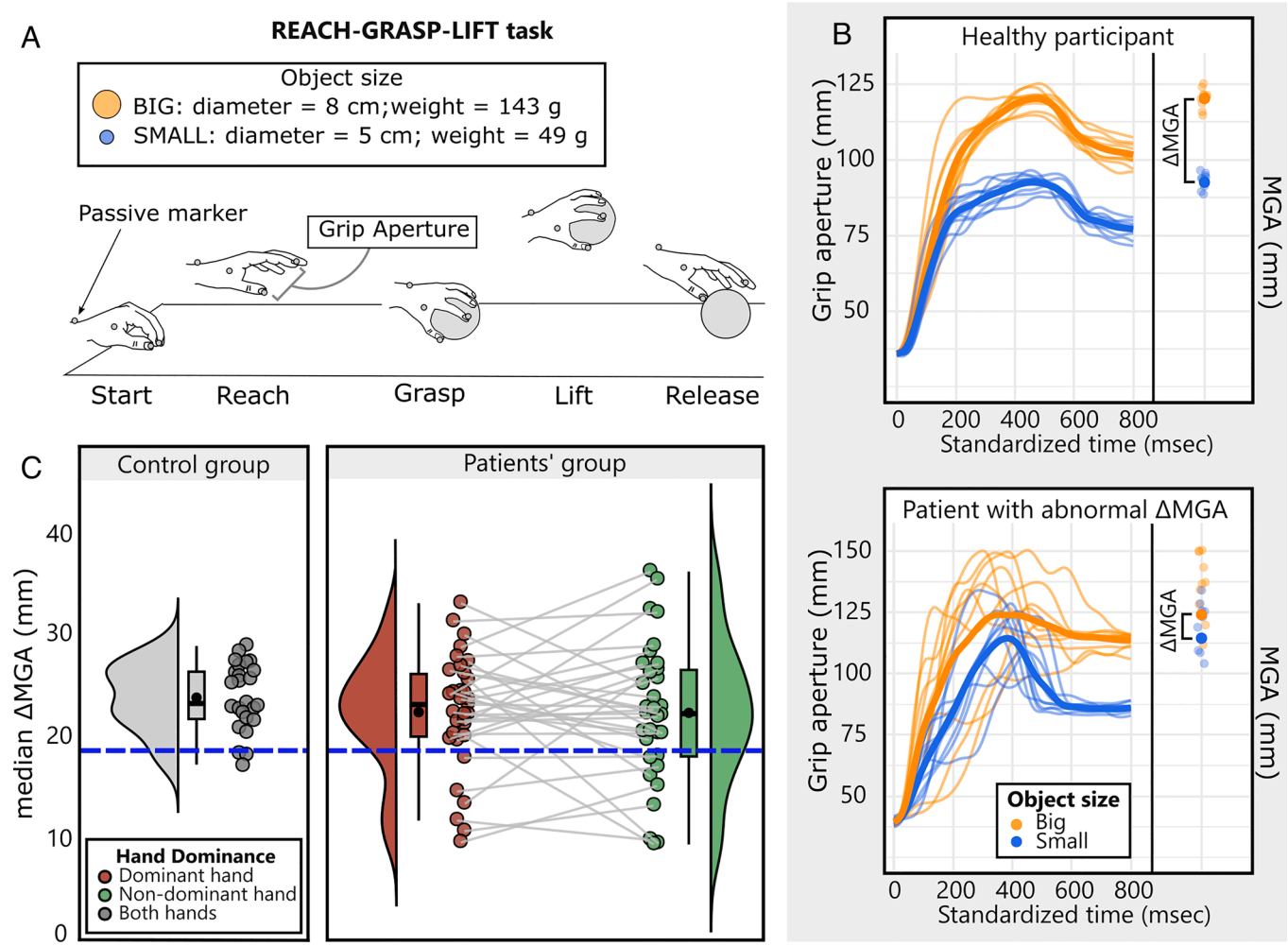

Fig. 1. Panel (*A*) schematization of the movement sequence of the task. The positions of the passive markers on the hand are indicated as small spheres. Panel (*B*) Example of individual recordings showing single trial data aligned to the start of movement (time = 0) ending with contact (grasping) with the object (excluding the lift phase). Lines indicate profiles of grip aperture (distance between thumb and index fingers) during the reach–grasp movements. Faint lines represent single trials and the solid lines represent the average profile. The dots indicate the values of maximum grip aperture (MGA) (i.e., the positive peak of the solid lines) of single trials (faint dots) and of the median of all trials (solid dots). The differential measure ΔMGA (the main experimental variable) is indicated by black square brackets, representing the difference between the median grip apertures for the big (8 cm) ball and for the small (5 cm) ball. The example patient (#7) shows abnormal values of ΔMGA. Panel (*C*) The plots illustrate the distribution of the ΔMGA values across the control group and the patients' group. The colored dots represent the median ΔMGA values for each individual, categorized in hand dominance for the patient group. The dashed horizontal line represents the cutoff for normality (ΔMGA = 18.4 mm). Violin plots indicate probability density functions of the distributions. Boxplots indicate minimum value, Q1, mean, median, Q3 and maximum value.

kinematics, representative of 2 different components of the reach–grasp action: 1) visuomotor integration related to object geometry, measured as the appropriateness of finger aperture during the reach phase (i.e., prior to contact with the object), in relation to object size, and by the peak velocity of grip aperture; 2) execution of the reaching movement toward the object, indexed by peak velocity of the wrist during the reach phase and by the reaching time. Individual deficits in patients were characterized by comparison with a control group of 21 healthy participants, resulting in individual binary categorizations in terms of normal or abnormal behaviors. Deficits were then related to specific lesion anatomy from presurgery MR scans, in a procedure of voxel-based lesion-symptom mapping (VBLSM) (38). This procedure assigns specific symptoms to specific brain voxels, with a statistical significance level. For the anatomical definition of statistical lesion maps, we referred to the Julich-Brain Atlas cytoarchitectonic maps (39) for cortical localizations and to the Tractotron atlas (40) of white matter bundles for white matter localizations. Both atlases are fed with spatial coordinates in a brain volume and attribute them probabilistically to specific cortical regions or to specific white matter tracts. Results showed that the appropriateness of hand preshaping to the target object is impaired following lesions of a very specific portion of the anterior ventral intraparietal sulcus (IPS), while the execution speed of finger opening required the integrity of a portion of the dorsal premotor cortex (PMd). Reaching behavior was impaired in association with lesions in the subcortical space involving fibers mainly in the first division of the superior longitudinal fasciculus (SLF-I).

Results

The study was approved by the Review Board for Ethics Committee for Clinical Trials of the University of Verona (Prog. 255CET) and was carried out in accordance with ethical standards of the Declaration of Helsinki (41). Written informed consent was obtained from all patients before starting the study. We included in the study a total of 33 eligible patients. A summary of demographic and clinical data is presented in Table 1. Patients were recruited within a narrow timeframe of approximately 4 d before the scheduled surgical procedure, closely aligned with the preoperative clinical and radiological assessment, including the acquisition of anatomical MR scans to be used for lesion analysis in the current protocol. The population's lesions had the following characteristics: the mean lesion size was 44.05 cm^3 (SD = 40.51, range = 1.12 to 158.39). Maximum lesions overlap corresponded to 13 lesions on a total of 33 lesions, centered at MNI coordinates $x = 23$; $y = -12$; $z = 41$, which corresponded to the MFC4 area of the middle frontal gyrus (map value = 0.0004). Lesion overlap is shown in Fig. 2. The specific VBLSM results for each kinematic parameter are summarized in the following paragraphs.

Finger Preshaping During Reaching. The capacity of the brain to transform visual information on an object's geometry is optimally captured by a differential measure of maximal finger aperture when grasping two objects of different sizes (36). Therefore, we considered as main variable of interest the ***Differential Maximum Grip Aperture (ΔMGA)*** between the 8 cm and the 5 cm ball, rather than the absolute value of MGA for each ball. ΔMGA is a highly invariant feature between subjects as witnessed by the data collected in healthy controls in the present study (see *SI Appendix*, Table S1 for normative data). ΔMGA was found to be abnormal in 10/33 patients. A representative example of both abnormal and normal grip aperture profile during grasping and the distribution of the ΔMGA values across the control group and the patients' group are shown in Fig. 1 *B* and *C*. The side of abnormal behavior was the contralesional in 4/10, ipsilesional in 1/10, and bilateral in 5/10. The unexpected pattern of unilateral ipsilesional deficit was observed in the only left-handed patient who was symptomatic. Considering only the 9 symptomatic right-handed patients, dominant hemisphere lesions produced bilateral deficits in 4/4 patients and contralateral deficits in 0/4 cases. Nondominant hemisphere lesions produced a clinical deficit only in the contralateral hand in 5/5 patients and bilateral deficits in 0/5 patients. This different effect of dominant vs. nondominant hemisphere lesions was statistically significant, $\chi^2(1, N = 9) = 9.00$, $P = 0.0027$. VBLSM procedures (Liebermeister statistics) indicated a CI (corrected $P < 0.05$) of $-2.51 > z < 3.475$, with 2,311 voxels surviving the threshold. The significant voxels were organized in 3 clusters in the anterior lateral intraparietal region. The center of mass of the volume was located at MNI coordinates of $x = 42$; $y = -35$; $z = 45$, corresponding to the hIP2 area of the IPS (map value = 0.50) on the Julich atlas. The location is illustrated in Fig. 3*A*. The peak z-value of the whole volume (z-peak = 4.48) was located 5 mm anteriorly to the center of mass, MNI coordinates of $x = 42$; $y = -32$; $z = 46$, corresponding to the postcentral sulcus, specifically to the border between Brodmann's area 2 (BA2) and the posterior parietal cortex. Three individual clusters were observed. The largest (2,042 voxels) was centered on the border between BA2, hIP2, and hIP3; the second largest (266 voxels) was centered between region PFcm and on area hIP2; and the third (3 voxels) was centered on area hIP2. Detailed anatomical descriptions of whole volume features are shown in Table 2. Anatomical descriptives of individual clusters are shown in *SI Appendix*, Table S2. The other parameter that we used as descriptor of the hand configuration for grasping was the ***Maximum Grip Aperture velocity (MGAV)***, which describes efficiency in executing the motor plan of hand shape configuration. Behavior was found to be abnormal in 9/33 patients. The side of abnormal behavior was contralesional in 5, ipsilesional in 2, and on both sides in 2 patients, with no specific association with the side of the lesion. VBLSM procedures (Liebermeister statistics) indicated a CI (corrected $P < 0.05$) of $-2.30 > z < 3.28$, with 2 voxels surviving the threshold, organized in a single cluster. The center of mass of the lesion volume was on the $x = 23$, $y = 2$, $z = 50$, and the peak activity corresponding to z-value = 3.65 was localized in the same coordinates $x = 23$, $y = 2$, $z = 50$, within the superior frontal sulcus, in proximity to the junction with the precentral sulcus. The coordinates corresponded to the premotor region 6d3 in the Julich atlas. The location is illustrated in Fig. 3*B*. Detailed anatomical descriptions of whole volume features are shown in Table 2.

Hand Transport During Reaching. The transport component of the reach–grasp movement was investigated by means of the peak wrist velocity during reaching and the total time of the reaching movement. ***Maximum Wrist Velocity during reaching (MWV-reach)*** was found to be abnormal in 11/33 patients. The side of abnormal behavior was contralesional in 6/11, and bilateral in 5/11, without any specific association with lesions in the dominant or nondominant hemisphere. VBLSM procedures (Liebermeister statistics) indicated a CI (corrected $P < 0.05$) of $-2.72 > z < 3.59$, with 182 voxels surviving the threshold, with a center of mass located at MNI coordinates of $x = 24$; $y = -16$; $z = 46$, located in the frontal lobe white matter. Comparison with the Julich atlas confirmed that no cortical region was associated

Table 1. Demographic and clinical data of patients with brain tumors

Patient ID	Age	Gender	Handedness	Affected hemisphere	Tumor localization	Tumor volume (cm3)	Edema volume (cm3)	Tumor histology (WHO classification)
1	74	M	Right-handed	Left	F	14.49	22.64	Glioblastoma (IV)
2	66	F	Right-handed	Right	F	12.31	158.39	Metastasis
3	58	M	Right-handed	Right	PTO	14.49	72.14	Glioblastoma (IV)
4	26	M	Right-handed	Left	F	3.55	-	Astrocytoma (II)
5	33	F	Right-handed	Right	FT	43.65	-	Astrocytoma (II)
6	51	M	Right-handed	Right	P	14.12	14.63	Gliosarcoma (IV)
7	61	M	Right-handed	Right	P	48.49	84.09	Glioblastoma (IV)
8	67	F	Right-handed	Right	F	33.24	94.03	Glioblastoma (IV)
9	37	M	Right-handed	Left	P	48.74	-	Astrocytoma (IV)
10	47	F	Right-handed	Left	F	7.89	13.11	Glioblastoma (IV)
11	68	M	Right-handed	Right	F	74.57	61.25	Glioblastoma (IV)
12	24	F	Right-handed	Right	F	7.73	-	Astrocytoma (II)
13	48	F	Right-handed	Right	P	35.01	123.89	Metastasis
14	61	M	Right-handed	Left	P	30.58	-	Glioblastoma (IV)
15	29	F	Right-handed	Right	F	4.31	6.23	Glioma low grade
16	50	F	Right-handed	Left	F	98.49	58.62	Glioma high grade
17	61	F	Right-handed	Right	P	5.54	-	Glioblastoma (IV)
18	66	M	Left-handed	Right	F	7.48	35.49	Glioblastoma (IV)
19	36	M	Right-handed	Right	F	90.16	-	Astrocytoma (II)
20	52	M	Right-handed	Left	F	18.57	113.63	Glioblastoma (IV)
21	51	M	Right-handed	Left	PTO	38.84	62.83	Gliosarcoma (IV)
22	61	F	Right-handed	Right	PO	18.95	17.77	Oligodendroglioma (II)
23	76	M	Right-handed	Left	P	18.96	-	Glioblastoma (IV)
24	66	F	Right-handed	Right	P	10.35	17.31	Glioblastoma (IV)
25	67	M	Right-handed	Right	P	39.29	63.14	Glioblastoma (IV)
26	41	M	Right-handed	Left	FT	23.82	20.92	Astrocytoma (II)
27	70	M	Right-handed	Left	FT	7.76	13.11	Glioblastoma (IV)
28	49	F	Right-handed	Left	F	1.12	-	Glioma low grade
29	54	M	Right-handed	Right	PO	21.33	49.73	Gliosarcoma (IV)
30	51	F	Right-handed	Right	P	3.246	5.54	Glioblastoma (IV)
31	53	M	Left-handed	Right	F	1.39	6.981	Glioblastoma (IV)
32	56	M	Left-handed	Left	PO	35.95	102,53	Glioblastoma (IV)
33	49	F	Right-handed	Right	PO	106.94	131,77	Glioblastoma (IV)

Abbreviations: P = parietal; PO = parieto-occipital; PTO = pariteto-temporo-occipital; F = frontal; FT= fronto-temporal.
Classification and grading relates to the WHO classification active when patients underwent surgery.

with the coordinate (maximum map value = 0.0004). The peak z-value (z-peak = 3.68) was located at MNI coordinates of $x = 21$; $y = -13$; $z = 54$ also located in the frontal white matter (Fig. 4).

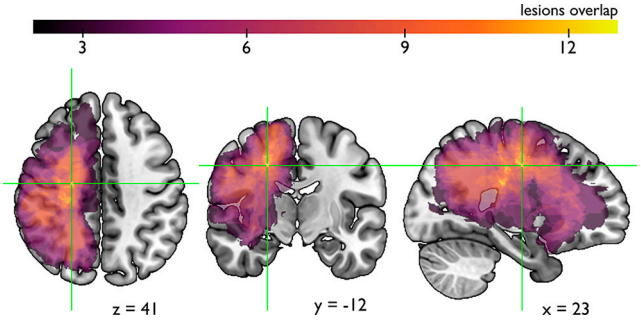

Fig. 2. Lesions overlay for the total sample of 33 patients. Superimposition of lesion volumes in standardized MNI space, on the standard MNI 152 brain. Color coding represents the number of lesions overlapping within each voxel. All lesions have been flipped on the right hemisphere. Only voxels with a minimum overlap of 2 patients are shown. The crosshairs indicate the location of the highest overlap value (n = 13) at the MNI coordinates x=23; y = −12; z = 41.

Disconnection analysis performed in Tractotron showed that the lesion volume affected with higher probability (100%) the first and the second divisions of the SLF (SLF-I and SLF-II), the corticospinal tract, and frontal commissural fibers. Significant voxels were distributed in 4 clusters of 81, 50, 48, and 3 voxels. The SPM Anatomy toolbox output showed that none of clusters 1,2 and 4 had significant location in the gray matter. Cluster 3 was mainly in the white matter, but near the gray matter in correspondence to the posterior bank of the central sulcus (area 3a of the Julich atlas). Detailed anatomical descriptions of whole volume features are shown in Table 2. Anatomical descriptives of individual clusters are shown in *SI Appendix*, Table S2. ***Movement Time (MT)*** was found to be abnormal in 14/33 patients. The abnormal behavior was bilateral in the majority (12/14 patients) and contralesional in 2/14 patients, without any specific association with the side of the lesion. VBLSM procedures failed to show significant results. Liebermeister measures indicated a CI (corrected $P < 0.05$) of $-3.09 > z < 3.62$ with 0 voxels surviving the threshold. Peak z-value of 3.1,

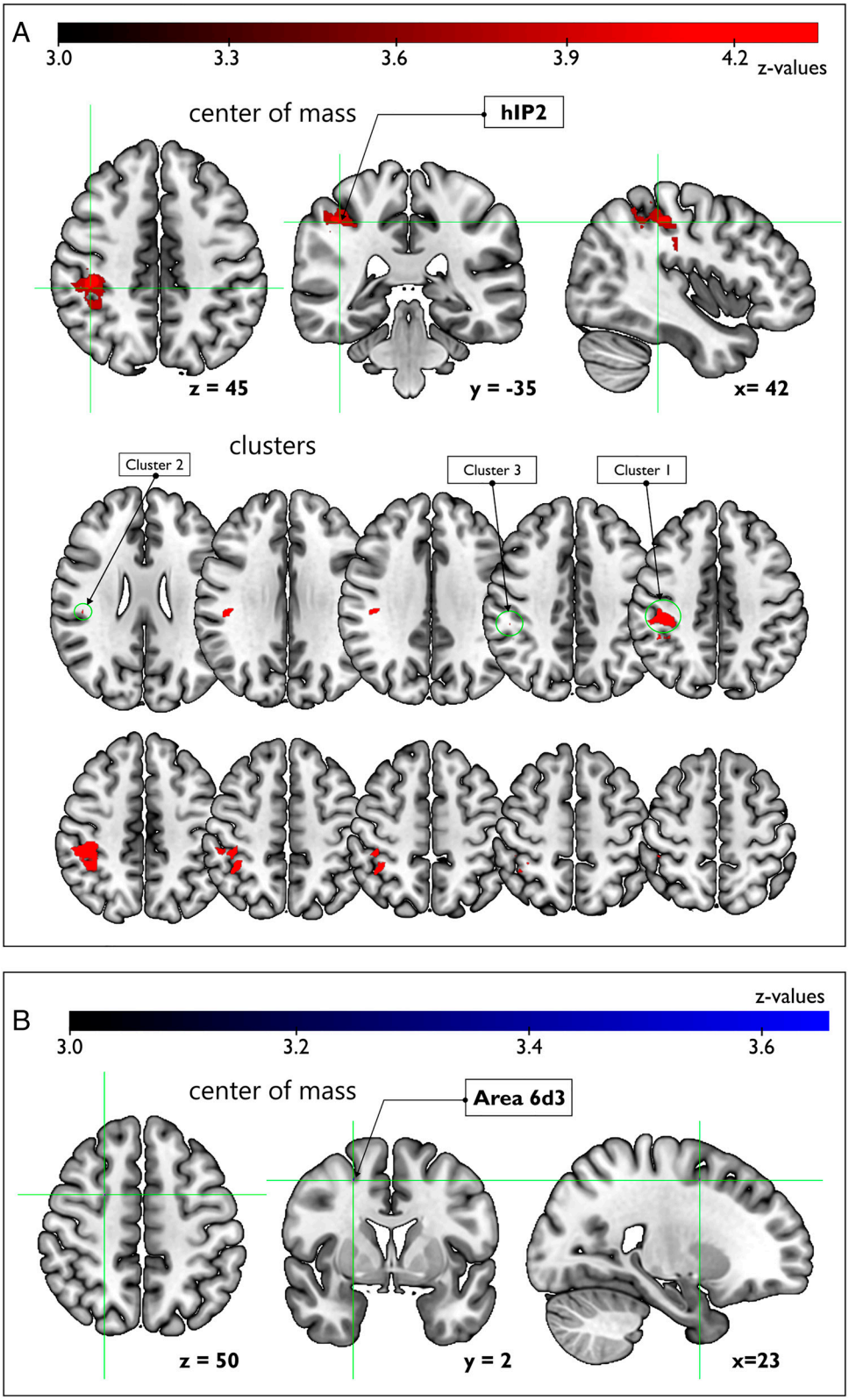

Fig. 3. VBLSM results for hand preshaping parameters. Panel (*A*) z-map of voxels significantly associated with MGA (ΔMGA) abnormalities. Z-values are thresholded to the z = 3.475, corresponding to p-value corrected for multiple comparisons of $P = 0.05$ and to uncorrected P value of $P = 2.5*10^{-4}$. Note that all single patient lesion volumes have been transposed on the right hemisphere. The *Upper* panel shows the significant lesion volume. The crosshair is centered on the MNI coordinates of the center of mass of the volume associated with abnormal ΔMGA. The arrow and labels indicate the anatomical assignment (Julich Atlas) of the center of mass. The *Bottom* panel shows the anatomical assignments of each cluster of significant voxels. The center of cluster 1 corresponded to the border between BA2, hIP2, and hIP3; the center of cluster 2 corresponded to region PFcm and the center of the third cluster corresponded to area hIP2 (all cortical parcels are referred to the Julich Atlas parcellation). See text for MNI coordinates. Panel (*B*) z-map of voxels significantly associated with deficits in MGAV. Z-values are thresholded to z = 3.28, corresponding to a *P*-value corrected for multiple comparisons of $P = 0.05$ and to an uncorrected *P*-value of $P = 5.1*10^{-4}$. The crosshair is centered on the MNI coordinates of the center of mass of the volume associate with abnormal MGAV). The arrow and label indicate the anatomical assignment.

Table 2. Anatomical characteristics of significant volumes associated with different motor deficits

Motor parameter	n.vox	Z-peak	*x*	*y*	*z*	Assignment on JLB atlas	Map value (JLB)	WM tract	Tract Dis. (%)
ΔMGA	2,311	4.34	42	−35	45	Area hIP2 (IPS)	0.497876		
						Area 2 (PostCS)	0.138241		
						Area hIP3 (IPS)	0.082139		
MGAV	2	3.65	23	2	50	Area 6d3 (SFS)	0.596729		
MWV-reach	182	3.68	21	−13	54			SLF-I	100
								SLF-II	100
								Corpus callosum	100
								Corticospinal tract	100
								Frontal commissural	100
								Pons	96
								Fronto Striatal	92
								Anterior thalamic projections	90
								Handinf U tract	78
								Handmid U tract	78

Abbreviations: nvox = number of significant voxels; WM = white matter; Tract Dis. (%) = tract disconnection probability. IPS = intraparietal sulcus; PostCS = postcentral sulcus. SFS = superior frontal sulcus.

Detailed anatomical descriptions of cortical regions associated with motor parameters. MNI coordinates of the volume's center of mass are reported. Anatomical areas were defined based on the Julich Brain Atlas (JLB). Map value describes the likelihood of the volume belonging to a given area. Only assignments with map values equal to or greater than 0.05 are reported. Volumes associated with MWV-reach deficits were located on the white matter; therefore, we report the tract intersected by the lesion map with higher probability of disconnection, as estimated by Tractotron atlas analysis. Tract disconnection probability indicates the probability that a given tract is interrupted by the lesion. Only values >75% are reported.

corresponding to an uncorrected *P*-value of $P = 0.001$ and a corrected *P*-value of $P = 0.65$.

Discussion

The present data show quantitative and causal evidence describing the anatomy and function of the grasping circuit in humans. We combined VBLSM with motion capture data in neuro-oncological patients. In this way, we investigated the anatomical localization of focal brain lesions according to their impact on specific kinematic parameters that characterize visually guided grasping. Patients had to reach, grasp, and lift one of two objects (spheres) of different sizes, alternatively with their dominant or nondominant hand. We analyzed kinematic parameters that characterize the 2 different components (grasp and reach) of such complex action. ΔMGA is the main marker of visuomotor transformations of the object geometry into appropriate hand postures (37) and MGAV expresses the execution of visuomotor plans. Conversely, MWV-reach and MT are relatively object-independent and instead indicating the capacity to reach for a spatial position (7). The results highlighted a mosaic of different brain regions in the parietal and frontal lobes (Fig. 5), each subserving a different function. The presence of ideomotor apraxia, deficits in verbal comprehension or weakness of the upper limb represented exclusion criteria. Therefore, clinical impairments presented here cannot be ascribed to neither higher-order disorders of action planning, to misinterpretation of the task, nor to elementary force deficits.

Deficits in Object-Dependent Visuomotor Transformations for Grasping. We show that to appropriately scale the finger grip to object size, humans require the integrity of a very specific single region in the anterior lateral bank of the IPS. The evidence is both quantitative and causal, being based on VBLSM procedures. According to the present findings, the phAIP is localized with the highest probability in hIP2 but also extending into a part of the adjacent hIP1 parcels of the intraparietal region as defined by Choi et al. (42), who suggested them as putative correlates of macaque AIP (hIP2) and Ventral Intraparietal (hIP1) areas. Our finding is in agreement with several functional neuroimaging studies in healthy participants (43). Indeed, the coordinates of phAIP from the present study overlap well with the peaks of BOLD activity from previous neuroimaging studies (e.g., Binkowski et al. (33) found peak activity in $x = -45$, $y = -38$, $z = 46$, Frey et al. (44) found peak activity in $x = -40$, $y = -36$, $z = 46$; Gallivan et al. (28) found activity in $x = 48$, u = −37, z = 45; Sartin et al. (45) found a cluster of activation in $x = -43$, $y = -37$, $z = 38$; all coordinates in MNI space). However, fMRI studies, besides activity in the phAIP region, show grasping-related activity within a large brain network, comprising the premotor and the supplementary motor areas, together with ventral visual stream regions, in the inferior temporal cortex (43). Such a network is likely to be indicative of corollary brain activity rather than causally based since we did not find any region other than the phAIP to be associated with ΔMGA. One unexpected finding in our study regards lateralization aspects of the hand preshaping function. We found that in the group of symptomatic right-handed patients (n = 9), lesions in the dominant (left) hemisphere (n = 4) selectively produced bilateral deficits, while nondominant hemisphere (right) lesions (n = 5) produced only contralesional hand-preshaping deficits. Previous studies have prevalently tested right-handed participants, all shown mainly contralateral deficits in reaching and grasping (33). Neuroimaging studies have reported both bilateral (27, 33, 46), and contralateral activation for reach–grasp (44). These data indicate a dominant role of the left hemisphere in encoding object shape for grasping since it seems that the left human AIP contains an object representation that is needed by both hands, while the right hemisphere receives a representation of the object that is strictly used for left-hand movements. The nonhuman primate model of the grasping circuit would have predicted a causal role in hand shaping formation also in the premotor cortex, as part of a parieto-frontal circuit. Indeed, the VBLSM analysis did show a premotor localization of lesional voxels associated with impaired (slower) execution of the specific finger aperture movement (and not of other movements). Such cluster of lesion

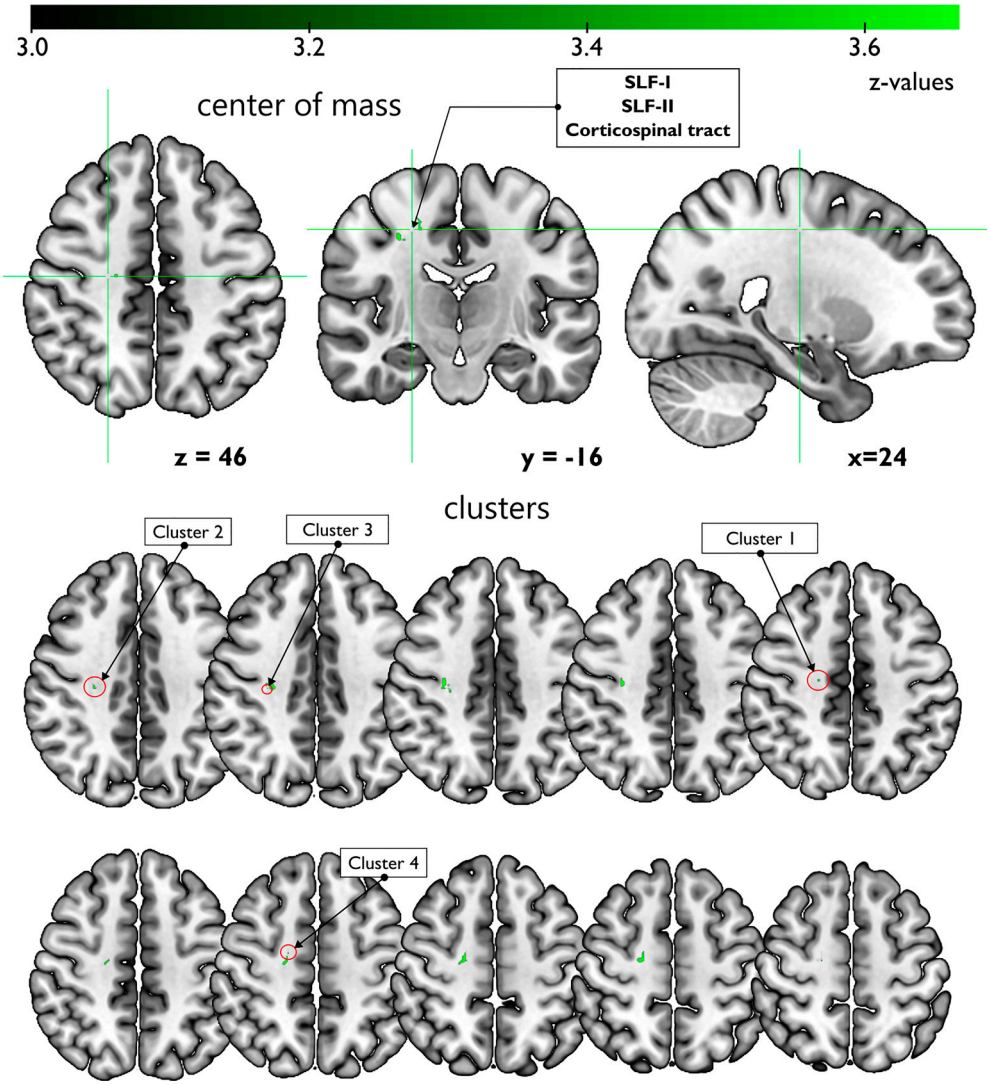

Fig. 4. VBLSM results for MWV-reach. Z-map of voxels significantly associated with MWV-reach abnormalities. Z-values are thresholded to the z = 3.59, corresponding to *P*-value corrected for multiple comparisons of $P = 0.05$ and to uncorrected *P* value of $P = 1.6*10^{-4}$. The upper figure shows the anatomical assignment and the MNI coordinates of the center of mass. The *Bottom* figure shows the anatomical assignments of each cluster of significant voxels. Clusters 1,2 and 4 were in the white matter. Cluster 3 was near the gray matter, in correspondence to the primary somatosensory cortex, Brodmann's area 3a.

voxels was localized in the dorsal sector of the premotor cortex, in correspondence of the junction between the superior frontal sulcus and the precentral sulcus, tightly overlapping the region where a premotor representation of visuomotor hand behavior has been found (47). Interestingly, we did not find significant localizations in the ventral premotor region, though previous data on healthy humans using noninvasive brain mapping techniques have shown that the ventral portion of the human precentral gyrus contains motor programs related to object-directed actions (9, 29–31, 36, 48) (26–28). While the current negative findings on the ventral premotor region in humans cannot actually exclude a functional role of PMv in object-directed grasping, they do indicate that the premotor activity associated with visually guided grasping involves also the dorsal sectors of the premotor region. Indeed, anatomical connectivity data in monkeys (6), and human functional neuroimaging (43) indicate that visually guided grasping is associated with multifocal activity in the premotor regions. A TMS experiment that investigated the very same experimental behavioral paradigm used here (36) showed that online TMS impairs hand preshaping when applied to a mosaic of both ventral and dorsal premotor regions. Finally, a significant contribution to the knowledge of cortical representation of object manipulation comes from intraoperative cortical stimulation in neurosurgical patients, during awake surgery procedures. It has been shown (45, 49) that a nonvisually guided manipulation task is impaired by stimulation of a multifocal complex of ventral and dorsal premotor regions, with distinct patterns of impairment. The current work is based on a hypothesis-independent whole-brain analysis, but in order to further explore the negative finding in the ventral premotor region, we performed a post hoc, region of interest (ROI)-based analysis (reported as supporting information) where we show that 8 patients had lesions overlapping the PMv and that only 2 of them were symptomatic in the ΔMGA measure and both had lesions extending in the parietal cortex. Half of them had abnormal MGA-velocity and all had lesions extending into the dorsal premotor region. In any case, given the current study design, the absence of ventral premotor localizations should be interpreted cautiously. Taken together, these results allow us to hypothesize a neural architecture for object-related grip aperture as follows: Visual information on object geometry for grasping is first constructed in the dominant (left) phAIP, which is then used directly for right-hand actions or transferred to the nondominant (right) hemisphere for left-hand actions. The object-related hand configuration represented in phAIP is then

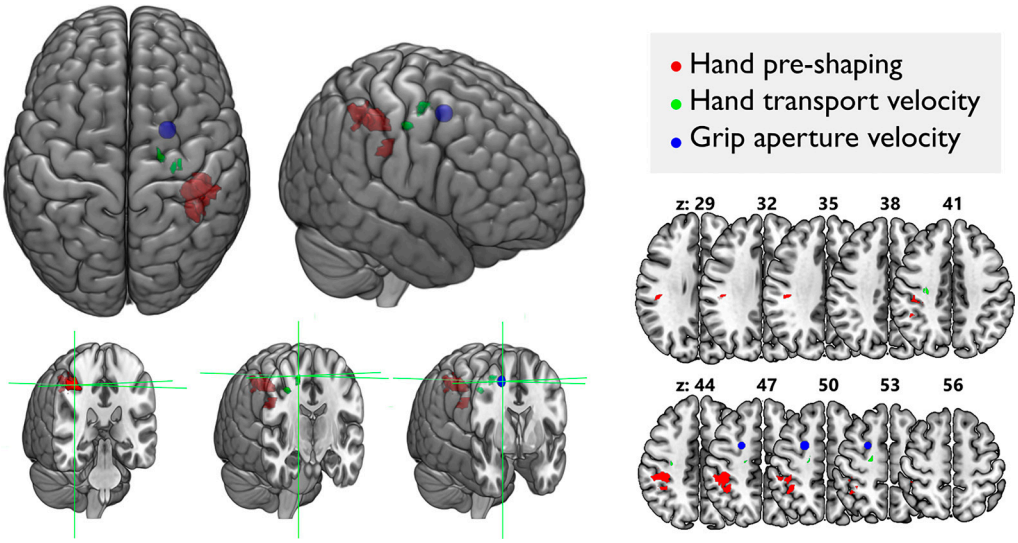

Fig. 5. Summary of brain volumes associated with abnormal kinematic parameters, superimposed on the MNI152 brain template. Note that the volume associated with abnormal MGAV values (color blue) consists of only 2 voxels and therefore, for illustration purposes, and only for this figure, has been inflated in a 5-voxel radius sphere. Axial section slices are shown on the right (MNI z-axis coordinates are indicated).

transferred to the ipsilateral premotor cortex, where the actual motor execution of the hand posture is represented, in terms of elementary kinematic features, such as velocity. In other words, phAIP has a unique role in representing object geometry in praxic terms, but the actual execution of the motor plan depends on the integrity of the PMd. A model of such a network is illustrated in Fig. 6. A recent neurophysiological investigation in monkeys has challenged the classical goal-oriented vocabulary of motor acts model of PMv organization thanks to ecologically valid recordings in freely moving animals. Lanzarini et al. (50) show that the neural representation of the actions is sparse rather than focal and is context dependent, concluding that premotor function is better explained in terms of dynamic cortical motor synergies rather than action goals. These findings are of paramount value in linking the present human data to nonhuman primate models. Coherently and in phylogenetic continuity with what proposed by Lanzarini et al. in monkeys, we found lesional effects compatible with execution of motor synergies rather than with representations of target objects, thereby supporting a holistic model of primate reaching-grasping control.

Deficits in Hand Transport During Reaching. Hand transport is a component of the reaching movement and is largely independent of the object geometry, as shown also in the present study in the data from normal participants. We found that most voxels significantly associated with abnormal MWV-reach were in the white matter, overlapping with the first division of the SLF-I, partly with SLF-II and with the corticospinal tract. The currently accepted model of the neural architecture of reaching movements postulates the building of a spatial representation of object position in the superior parietal lobule, which is supposedly transferred by means of the SLF-I to the PMd, where the reaching motor plan involving proximal limb muscles is implemented (51, 52). Previous lesional studies investigating misreaching or optic ataxia indicate that lesions of the superior parietal lobule (53, 54), cause deficits in reaching accuracy. The present data show that the implementation of reaching plans in an actual movement relies on a dorsal network and specifically requires the integrity of the dorsal part of the SLF, corresponding largely to SLF-I. The probable reason why we did not find parietal localizations for reaching is that we did not perform a full investigation of spatially oriented behavior as is commonly used to define optic ataxia. Indeed, we did not investigate different spatial positions of the target.

Conclusions. Our work draws a clear anatomically based model of the different components of the reach–grasp networks in the human brain and it does so by establishing quantitative causal relations between different nodes in the network and different behavioral components of the action. Within the grasping network, we show a clear double dissociation between finger aperture, represented in the phAIP, and the movement required to obtain such finger aperture, represented in PMd. This finding is at odds with expectations from previous models, which postulate a role of the PMv in object-directed grasping. In addition, we observed a seemingly unique human feature, i.e., a left-hemispheric

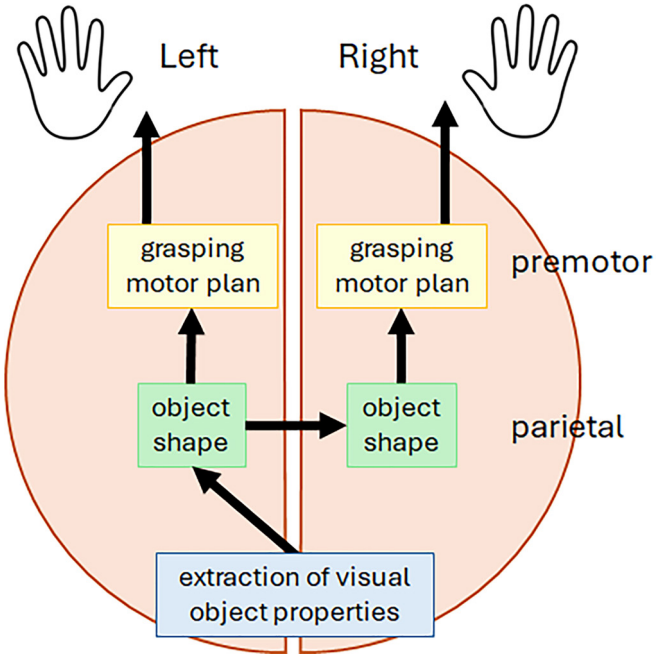

Fig. 6. Model of processing of object-related visual information in humans that takes into account the lateralization hypothesis and the division of labor between the parietal and the premotor cortices.

dominance for the praxic representation of object geometry in the parietal lobe.

Materials and Methods

Participants. We screened for enrollment in the study all patients scheduled for elective brain tumor surgery in the Neurosurgical Unit of the Verona University Hospital. Inclusion criteria were radiological evidence of a single supratentorial brain tumor (primitive or metastatic); age between 18 and 80 y; and spared verbal comprehension. Exclusion criteria were weakness of the contralesional upper limb evaluated by maximum grip force (55) measured with an electronic hand-held dynamometer (Camry model EH 101); apraxia; concurrent medical conditions that potentially influence data analysis and hinder participation in the study (e.g., amputation); psychiatric disorders; dementia; and radiological evidence of meningioma. Of 74 patients, 33 satisfied inclusion criteria and agreed to be enrolled in the study. The patients' demographics were as follows: 19 Male (mean age = 53.30 y, SD = 13.72 y, range 24 to 76); mean education = 11.91 y (SD = 3.11 y, range 8 to 18). The patient's handedness was evaluated with the Edinburgh Handedness Inventory (56). A comprehensive cognitive screening was performed by a qualified neuropsychologist a few days before surgery, assessing the following cognitive domains: praxis, verbal memory (both short-term and long-term), spatial memory (both short-term and long-term), selective and divided attention, executive functions, language abilities, and visuospatial skills. For the creation of normal values, 25 healthy volunteer participants (12 Male, mean age = 47.2 y, SD = 16.9 y, range 23 to 82; mean education = 17.8 y, SD = 3.98 y, range = 11 to 25) were recruited as a group control, matched to the patient cohort for age distribution $t(56) = 1.55$, $P = 0.13$, and gender ratio $\chi^2(1) = 0.52$, $P = 0.47$. All volunteer participants but three were right-handed.

Motion Capture. The upper limb's kinematics were measured using a 7-camera 3D optical (near infrared) motion capture system (FLEX13 – Optitrack; NaturalPoint Inc., Corvallis, OR). Before recording, the system was calibrated with a mean error of 0.39 mm. The cameras were distant ~1.8 m from the working space and sampled at 120 Hz. Four passive infrared reflecting markers with a diameter of 9.5 mm were attached to the wrist (apophysis of the ulna), on the tips of the thumb and index fingers (directly upon the finger nail), and on the distal part of the second metacarpal bone of both hands.

Behavioral Task. Participants sat in front of a table on which one of two objects (large – 8 cm in diameter, weight: 143 gr- and small – 5 cm in diameter, weight: 49 gr – wooden spheres of identical texture) were placed along their midsagittal plane. The distance from the object was determined individually as 70% of the functional participant's arm length. Each trial began with the participant's hand on the start position (20 cm lateral to the midsagittal plane), with the thumb and index finger touching together. Patients and healthy controls performed, upon receiving of a "go" signal, a reach–grasp–lift action (Fig. 1*A*). Emphasis was explicitly put on spontaneity and accuracy of the action rather than on speed. The task consisted of two blocks in which the participant performed the task with one hand or the other, in a between-participant randomized block order. Each block consisted of twenty trials, with ten trials for each of the two objects, in random order. Objects were manually changed by the experimenter. Overall, the reach-to-grasp task lasted for around 15 min, including the setup time.

Preprocessing of Kinematic Data. Motion capture data were processed using custom code written in the R software (version 4.0.4, R Core Team, 2021) (57). Data from each trial were filtered with a 5th-order Butterworth 12-Hz low-pass filter. The wrist marker was used to estimate the movement onset with an automatic recognition algorithm (58). We extracted the following kinematic parameters from each reach–grasp movement: A) Measures of hand preshaping during reach: 1) MGA, which represents the maximum distance between the markers on the thumb and index fingers during the reaching phase; 2) MGAV, which represents the peak of the profile of the grip aperture velocity. B) Measures of efficiency of the transport of the hand to the desired position (reaching phase): 1) MT, which is the time between the wrist movement onset and the end of the reaching (i.e., the end of the wrist movement corresponded to the contact with the object); 2) Maximum Wrist Velocity (MWV-reach), which is the peak of wrist velocity profile before touching the object. In this way, each trial was characterized by four kinematic measures. The following step consisted in calculating the median value (which was preferred to the mean value due to the small numerosity of repetitions per each condition) of each of the six parameters in each of the 4 conditions of interest, corresponded to the 4 cells of the 2 × 2 experimental design: two objects (5 cm or 8 cm) and 2 hands (left or right). Finally, limited to the MGA measure, we calculated the difference between the MGA median values for the 8 cm minus the 5 cm ball trials (referred to as ΔMGA), which was used as experimental variable (Fig. 1*B*), rather than the raw MGA. The same preprocessing procedures were applied to the group of patients and to healthy participants.

Statistical Analysis of Kinematic Data. The purpose of the analysis was to classify each patient's kinematic parameters as impaired or normal. Due to lack of standardization and of normative values, we produced our own ranges of normality using the data from healthy participants, by calculating the mean ± 1.64 SD (i.e., the 5th and 95th percentile point in the normal distribution) confidence limits (reported in *SI Appendix*, Table S1). We defined normal intervals separately for each hand (dominant or nondominant) and ball size (5 or 8) if a significant difference between those factors was found in the healthy controls, otherwise, normal values were produced collapsing the side and ball factors. The patient's behavior was evaluated as normal or abnormal, separately for each hand. Additionally, we used chi-square statistics to analyze the differences between the side of the deficit (contralesional, ipsilesional, bilateral) and the hemispheric localization of the lesion (dominant, nondominant).

MRI Structural Data. MRI scans of each patient's brain were acquired as part of the presurgery routine on a 3 T scanner with an eight-channel head coil (Signa 3 T, General Electric Healthcare, Milwaukee, USA). T1-weighted 3D MPRAGE images were acquired using the following parameters (echo train length: 1, TE: 2.67 ms, TR: 2.000, matrix size: 256 × 246, slice thickness: 1 mm). T2-weighted, FLAIR images were also acquired (TR 6,000 ms, TE 150mss, TI 15 Neuro-Connect 2,000 ms). All images were acquired on average at a 4.7-d interval from the clinical and kinematic evaluation, thus representing a simultaneous snapshot of the lesion extension.

VBLSM Analysis. We used VBLSM to associate behavioral deficits to specific lesion voxels (59). First, we defined in each patient the lesion volume. To do so, individual MR scans were normalized to the Montreal Neurological Institute (MNI) standard space using SPM12 software (Wellcome Trust Centre for Neuroimaging, London). For each patient, the volume of interest corresponding to the lesions was generated using a semiautomatic cluster segmentation approach with the ITK-SNAP software (60) (available at www.itksnap.org), manually inspected, and refined by the first author (V.D.C.), and systematically checked by the last author (L.C.). The result of the segmentation procedures includes separated lesion and edema volumes. For the purposes of the present work, we decided to consider as volume of interest both lesion and edema, when edema was present. Although tissues affected by edema may experience less severe functional impairment than the actual lesion volume, it is well accepted that edematous tissue is not functioning optimally. From a risk/benefit perspective, the potential risk of excluding edema outweighs that of including it because it would mean treating tissue that is nonoptimally functioning as normal, potentially overlooking its contribution to the behavioral dysfunction. Aligned with this, previous studies in humans have demonstrated the significant impact of edema on cognitive functions (61, 62). There is agreement, especially in acute or rapidly developing lesions such as high-grade gliomas, that edema, when present, should be considered as malfunctioning brain volume (63, 64). Indeed, it is common practice to include edema in lesion volumes when performing VBLSM in oncological patients (65, 66). All lesions were flipped along the *x*-axis to the right hemisphere to increase numerosity and therefore statistical power. VBLSM was performed using the NiiStat software (https://www.nitrc.org/projects/niistat/). Whole brain analyses were performed separately for each of the 4 kinematic parameters, that were classified binarily in each patient as normal or abnormal. We used the Normal Permutation method (67) with 3,000 permutations, to correct for false positives. Only voxels involved in 20% (n = 6) or more patients were considered. Significance threshold was set to $P = 0.05$ (corrected for multiple comparison). Once a brain volume was found to be significantly associated with a behavioral deficit, we mapped the coordinates of the cortical lesions on the Julich-Brain Atlas, cytoarchitectonic maps version 3.1 (39). We a) calculated the center of mass of the lesion on MRIcron software (NITRC, http://www.nitrc.org/projects/mricron) and determined the probability values (i.e., map value) of cytoarchitectonic regions at the lesion center of mass MNI coordinates by using the siibra toolsuite (68); the same assignment was

made with respect the z-peak of threshold maps; and b) we made a volume-based analysis by means of the SPM Anatomy toolbox 3.0 (69) which refers to the same standard atlas, for the anatomical description of volume's clusters. When assignments were not available in the cytoarchitectonic maps, because the statistical lesion maps fell in the white matter, we used Tractotron software as part of the BCB toolkit (http://www.toolkit.bcblab.com), (40) to quantify the severity of disconnection by measuring the probability of the tract to be disconnected by the lesion. For each statistical lesion maps, tracts with a probability of disconnection higher than 50% were considered disconnected (70).

Data, Materials, and Software Availability. Anonymized behavioral and radiological data are freely available in the OSF repository https://osf.io/h4xfu/ (71).

ACKNOWLEDGMENTS. This work was supported by the CaRiVerona foundation (awarded to F.S. for the project "Neuro-Connect - Systems neuroscience meets clinical neurosurgery: development of novel multimodal monitoring indices of brain connectivity in patients with glioma" ID ROL10768 COD.SIME 2018.0911) and the Fondazione ASINO per la neurochirurgia oncologica (grant to V.D.C. for the project: "Voluntary motor control in neuro-oncological patients").

1. J. M. Karl, I. Q. Whishaw, Different evolutionary origins for the reach and the grasp: An explanation for dual visuomotor channels in primate parietofrontal cortex. *Front. Neurol.* **4**, 1–13 (2013).
2. G. Rizzolatti, L. Cattaneo, M. Fabbri-Destro, S. Rozzi, Cortical mechanisms underlying the organization of goal-directed actions and mirror neuron-based action understanding. *Physiol. Rev.* **94**, 655–706 (2014).
3. R. Caminiti, G. M. Innocenti, A. Battaglia-Mayer, Organization and evolution of parieto-frontal processing streams in macaque monkeys and humans. *Neurosci. Biobehav. Rev.* **56**, 73–96 (2015).
4. E. Borra, M. Gerbella, S. Rozzi, G. Luppino, The macaque lateral grasping network: A neural substrate for generating purposeful hand actions. *Neurosci. Biobehav. Rev.* **75**, 65–90 (2017).
5. A. Belmalih *et al.*, Multimodal architectonic subdivision of the rostral part (area F5) of the macaque ventral premotor cortex. *J. Comp. Neurol.* **512**, 183–217 (2009).
6. M. Lanzilotto *et al.*, Anterior intraparietal area: A hub in the observed manipulative action network. *Cereb. Cortex* **29**, 1816–1833 (2019).
7. M. Jeannerod, M. A. Arbib, G. Rizzolatti, H. Sakata, Grasping objects: The cortical mechanisms of visuomotor transformation. *Trends Neurosci.* **18**, 314–320 (1995).
8. F. Maule, G. Barchiesi, T. Brochier, L. Cattaneo, Haptic working memory for grasping: The role of the parietal operculum. *Cereb. Cortex* **25**, 528–537 (2015).
9. L. Cattaneo, F. Maule, D. Tabarelli, T. Brochier, G. Barchiesi, Online repetitive transcranial magnetic stimulation (*TMS*) to the parietal operculum disrupts haptic memory for grasping. *Hum. Brain Mapp.* **36**, 4262–4271 (2015).
10. S. Schaffelhofer, H. Scherberger, Object vision to hand action in macaque parietal, premotor, and motor cortices. *eLife* **5**, e15278 (2016).
11. L. Fogassi *et al.*, Cortical mechanism for the visual guidance of hand grasping movements in the monkey: A reversible inactivation study. *Brain* **124**, 571–586 (2001).
12. V. Raos, Functional properties of grasping-related neurons in the ventral premotor area F5 of the macaque monkey. *J. Neurophysiol.* **95**, 709–729 (2005).
13. M. A. Baumann, M.-C. Fluet, H. Scherberger, Context-specific grasp movement representation in the macaque anterior intraparietal area. *J. Neurosci.* **29**, 6436–6448 (2009).
14. A. Murata, V. Gallese, G. Luppino, M. Kaseda, H. Sakata, Selectivity for the shape, size, and orientation of objects for grasping in neurons of monkey parietal area AIP. *J. Neurophysiol.* **83**, 2580–2601 (2000).
15. M. C. Romero, P. Janssen, Receptive field properties of neurons in the macaque anterior intraparietal area. *J. Neurophysiol.* **115**, 1542–1555 (2016).
16. H. Sakata *et al.*, Neural coding of 3D features of objects for hand action in the parietal cortex of the monkey. *Philos. Trans. R. Soc. Lond. B Biol. Sci.* **353**, 1363–1373 (1998).
17. G. Rizzolatti *et al.*, Neurons related to goal-directed motor acts in inferior area 6 of the macaque monkey. *Exp. Brain Res.* **67**, 220–224 (1987).
18. R. W. Intveld, B. Dann, J. A. Michaels, H. Scherberger, Neural coding of intended and executed grasp force in macaque areas AIP, F5, and M1. *Sci. Rep.* **8**, 17985 (2018).
19. J. A. Michaels, H. Scherberger, Population coding of grasp and laterality-related information in the macaque fronto-parietal network. *Sci. Rep.* **8**, 1710 (2018).
20. R. P. Dum, P. L. Strick, Frontal lobe inputs to the digit representations of the motor areas on the lateral surface of the hemisphere. *J. Neurosci.* **25**, 1375–1386 (2005).
21. G. Prabhu *et al.*, Modulation of primary motor cortex outputs from ventral premotor cortex during visually guided grasp in the macaque monkey. *J. Physiol.* **587**, 1057–1069 (2009).
22. H. Shimazu, M. A. Maier, G. Cerri, P. A. Kirkwood, R. N. Lemon, Macaque ventral premotor cortex exerts powerful facilitation of motor cortex outputs to upper limb motoneurons. *J. Neurosci.* **24**, 1200–1211 (2004).
23. P. L. Strick, C. C. Kim, Input to primate motor cortex from posterior parietal cortex (area 5). I. Demonstration by retrograde transport. *Brain Res.* **157**, 325–330 (1978).
24. L. Cattaneo, D. Giampiccolo, P. Meneghelli, V. Tramontano, F. Sala, Cortico-cortical connectivity between the superior and inferior parietal lobules and the motor cortex assessed by intraoperative dual cortical stimulation. *Brain Stimul.* **13**, 819–831 (2020).
25. O. A. Gharbawie, I. Stepniewska, H. Qi, J. H. Kaas, Multiple parietal-frontal pathways mediate grasping in macaque monkeys. *J. Neurosci.* **31**, 11660–11677 (2011).
26. C. Cavina-Pratesi *et al.*, Human neuroimaging reveals the subcomponents of grasping, reaching and pointing actions. *Cortex* **98**, 128–148 (2018).
27. J. C. Culham *et al.*, Visually guided grasping produces fMRI activation in dorsal but not ventral stream brain areas. *Exp. Brain Res.* **153**, 180–189 (2003).
28. J. P. Gallivan, D. A. McLean, K. F. Valyear, C. E. Pettypiece, J. C. Culham, Decoding action intentions from preparatory brain activity in human parieto-frontal networks. *J. Neurosci.* **31**, 9599–9610 (2011).
29. M. Davare, K. Montague, E. Olivier, J. C. Rothwell, R. N. Lemon, Ventral premotor to primary motor cortical interactions during object-driven grasp in humans. *Cortex* **45**, 1050–1057 (2009).
30. T. Bäumer *et al.*, Inhibitory and facilitatory connectivity from ventral premotor to primary motor cortex in healthy humans at rest – A bifocal TMS study. *Clin. Neurophysiol.* **120**, 1724–1731 (2009).
31. E. R. Buch, R. B. Mars, E. D. Boorman, M. F. S. Rushworth, A network centered on ventral premotor cortex exerts both facilitatory and inhibitory control over primary motor cortex during action reprogramming. *J. Neurosci.* **30**, 1395–1401 (2010).
32. H. J. Freund, H. Hummelsheim, Lesions of premotor cortex in man. *Brain* **108**, 697–733 (1985).
33. F. Binkofski *et al.*, Human anterior intraparietal area subserves prehension: A combined lesion and functional MRI activation study. *Neurology* **50**, 1253–1259 (1998).
34. V. Gallese, A. Murata, M. Kaseda, N. Niki, H. Sakata, Deficit of hand preshaping after muscimol injection in monkey parietal cortex. *Neuroreport* **5**, 1525–1529 (1994).
35. D. A. Nowak, The impact of stroke on the performance of grasping: Usefulness of kinetic and kinematic motion analysis. *Neurosci. Biobehav. Rev.* **32**, 1439–1450 (2008).
36. C. Lega *et al.*, The topography of visually-guided grasping in the premotor cortex: A dense-transcranial magnetic stimulation (*TMS*) mapping study. *J. Neurosci.* **40**, 6790–6800 (2020), 10.1523/jneurosci.0560-20.2020.
37. M. Jeannerod, The formation of finger grip during prehension. A cortically mediated visuomotor pattern. *Behav. Brain Res.* **19**, 99–116 (1986).
38. J. V. Baldo, M. V. Ivanova, T. J. Herron, S. M. Wilson, N. F. Dronkers, "Voxel-Based Lesion Symptom Mapping" in *Lesion-to-Symptom Mapping: Principles and Tools, Neuromethods*. D. Pustina, D. Mirman, Eds. (Springer, US, 2022), pp. 95–118.
39. K. Amunts, H. Mohlberg, S. Bludau, K. Zilles, Julich-Brain: A 3D probabilistic atlas of the human brain's cytoarchitecture. *Science* **369**, 988–992 (2020).
40. C. Foulon *et al.*, Advanced lesion symptom mapping analyses and implementation as BCBtoolkit. *GigaScience* **7**, 1–17 (2018).
41. World Medical Association, World medical association declaration of helsinki: Ethical principles for medical research involving human subjects. *JAMA* **310**, 2191–2194 (2013).
42. H.-J. Choi *et al.*, Cytoarchitectonic identification and probabilistic mapping of two distinct areas within the anterior ventral bank of the human intraparietal sulcus. *J. Comp. Neurol.* **495**, 53–69 (2006).
43. S. Sartin, M. Ranzini, C. Scarpazza, S. Monaco, Cortical areas involved in grasping and reaching actions with and without visual information: An ALE meta-analysis of neuroimaging studies. *Curr. Res. Neurobiol.* **4**, 100070 (2023).
44. S. H. Frey, D. Vinton, R. Norlund, S. T. Grafton, Cortical topography of human anterior intraparietal cortex active during visually guided grasping. *Cogn. Brain Res.* **23**, 397–405 (2005).
45. L. Fornia *et al.*, Direct electrical stimulation of premotor areas: Different effects on hand muscle activity during object manipulation. *Cereb. Cortex* **30**, 391–405 (2020).
46. C. Grefkes, P. H. Weiss, K. Zilles, G. R. Fink, Crossmodal processing of object features in human anterior intraparietal cortex: An fMRI study implies equivalencies between humans and monkeys. *Neuron* **35**, 173–184 (2002).
47. C. Amiez, P. Kostopoulos, A.-S. Champod, M. Petrides, Local morphology predicts functional organization of the dorsal premotor region in the human brain. *J. Neurosci.* **26**, 2724–2731 (2006).
48. F. Fiori, E. Chiappini, A. Avenanti, Enhanced action performance following TMS manipulation of associative plasticity in ventral premotor-motor pathway. *NeuroImage* **183**, 847–858 (2018).
49. L. Viganò *et al.*, Stimulation of frontal pathways disrupts hand muscle control during object manipulation. *Brain* **145**, 1535–1550 (2022).
50. F. Lanzarini *et al.*, Neuroethology of natural actions in freely moving monkeys. *Science* **387**, 214–220 (2025).
51. C. Cavina-Pratesi *et al.*, Functional magnetic resonance imaging reveals the neural substrates of arm transport and grip formation in reach-to-grasp actions in humans. *J. Neurosci.* **30**, 10306–10323 (2010), 10.1523/JNEUROSCI.2023-10.2010.
52. J. C. Culham, K. F. Valyear, Human parietal cortex in action. *Curr. Opin. Neurobiol.* **16**, 205–212 (2006).
53. R. A. Andersen, C. A. Buneo, Intentional maps in posterior parietal cortex. *Annu. Rev. Neurosci.* **25**, 189–220 (2002).
54. Y. Rossetti, L. Pisella, *Optic Ataxia: Beyond The Dorsal Stream Cliché* (Elsevier B.V, ed. 1, 2018).
55. A. W. Andrews, M. W. Thomas, R. W. Bohannon, Normative values for isometric muscle force measurements obtained with hand-held dynamometers. *Phys. Ther.* **76**, 248–259 (1996).
56. R. C. Oldfield, The assessment and analysis of handedness: The Edinburgh inventory. *Neuropsychologia* **9**, 97–113 (1971).
57. R Core Team, R: A language and environment for statistical computing. (R Core Team, Vienna, 2021).
58. N. Teasdale, C. Bard, M. Fleury, D. E. Young, L. Proteau, Determining movement onsets from temporal series. *J. Mot. Behav.* **25**, 97–106 (1993).
59. E. Bates *et al.*, Voxel-based lesion-symptom mapping. *Nat. Neurosci.* **6**, 448–450 (2003).
60. P. A. Yushkevich *et al.*, User-guided 3D active contour segmentation of anatomical structures: Significantly improved efficiency and reliability. *NeuroImage* **31**, 1116–1128 (2006).
61. Y. Lampl, Y. Barak, A. Achiron, I. Sarova-Pinchas, Intracranial meningiomas: Correlation of peritumoral edema and psychiatric disturbances. *Psychiatry Res.* **58**, 177–180 (1995).
62. S. Steinvorth *et al.*, Neuropsychological outcome after fractionated stereotactic radiotherapy (FSRT) for base of skull meningiomas: A prospective 1-year follow-up. *Radiother. Oncol.* **69**, 177–182 (2003).
63. S. M. Sheppard, A. L. C. Schneider, A. E. Hillis, "Defining the Lesion for Lesion-Symptom Mapping" in *Lesion-to-Symptom Mapping: Principles and Tools*, D. Pustina, D. Mirman, Eds. (Springer, US, 2022), pp. 1–26.
64. E. E. van Grinsven *et al.*, The impact of etiology in lesion-symptom mapping - A direct comparison between tumor and stroke. *Neuroimage Clin.* **37**, 103305 (2023).
65. F. Campanella, M. Skrap, A. Vallesi, Speed-accuracy strategy regulations in prefrontal tumor patients. *Neuropsychologia* **82**, 1–10 (2016).
66. V. Tarantino *et al.*, Impaired cognitive control in patients with brain tumors. *Neuropsychologia* **169**, 108187 (2022).

67. A. M. Winkler, G. R. Ridgway, M. A. Webster, S. M. Smith, T. E. Nichols, Permutation inference for the general linear model. *NeuroImage* **92**, 381–397 (2014).
68. siibralab. (2023), https://it.mathworks.com/matlabcentral/fileexchange/121148-siibralab [Accessed 28 July 2024].
69. S. B. Eickhoff *et al.*, Assignment of functional activations to probabilistic cytoarchitectonic areas revisited. *NeuroImage* **36**, 511–521 (2007).
70. M. Thiebaut de Schotten *et al.*, Damage to white matter pathways in subacute and chronic spatial neglect: A group study and 2 single-case studies with complete virtual "in vivo" tractography dissection. *Cereb. Cortex* **24**, 691–706 (2014).
71. L. Cattaneo, V. Di Caro, Data from "The neural bases of the reach–grasp movement in humans: Quantitative evidence from brain lesions". Open Science Framework (OSF). https://osf.io/h4xfu/. Deposited 15 February 2025.